**SUPPORTING INFORMATION**

# Joint Contribution of Spatiotemporal Factors and Chemical Composition on the Hygroscopicity of Aerosol Particles in the Southern Great Plains

Kyle McCary[1] , Rylen Pereira[1] , Alan Gonzalez[2] , Xiangxinyue Meng[1] , Ajith Thenoor Chandran[1], Heewon Yim[2] , Maria Zawadowicz[3] , John E. Shilling[4] , Qi Ying[2] , Yue Zhang[1,*]

[1]*Department of Atmospheric Sciences, Texas A&M University, College Station, TX, 77843, USA*

[2]*Zachry Department of Civil and Environmental Engineering, Texas A&M University, College Station, TX, 77843, USA*

[3]*Brookhaven National Laboratory, Upton, NY, 11973, USA*

[4]*Pacific Northwest National Laboratory, Richland, WA, 99354, USA*

October 2026

*Atmospheric Chemistry and Physics*

[*]*Corresponding author:* Yue Zhang, yuezhang@tamu.edu

No. of pages: 26

No. of figures: 13

No. of tables: 5

## Section S1. Consistency of FIMS Mobility and AMS Vacuum Aerodynamic Diameters

The FIMS reports the electrical mobility diameter ($d_m$), whereas the HR-ToF-AMS aerodynamic lens transmits and sizes particles by their vacuum aerodynamic diameter ($d_{va}$), meaning that the two are not numerically equal. In order to make sure both the FIMS and the AMS describe the same particles over the size range relevant to activation, corrective calculations and checks were conducted. Following *DeCarlo et al.*, both diameters relate to the volume-equivalent diameter $d_{ve}$ through $d_{va} = (\rho_p/\rho_0)(1/\chi_v)\, d_{ve}$ and $d_m = \chi_t\, d_{ve}$, where $\rho_p$ is the particle density, $\rho_0 = 1$ g cm$^{-3}$, and $\chi_v$ and $\chi_t$ are the free-molecular and transition-regime dynamic shape factors (DeCarlo et al., 2004). The aerosol sampled during HI-SCALE is expected to be near-spherical, we adopt $\chi_v = \chi_t = 1$, which gives Eq. S1:

$$d_m = d_{va}\, \rho_0 / \rho_p \quad \text{(S1)}$$

The particle density was estimated from the measured AMS composition. Using the campaign-mean elemental ratios (O:C = 0.44, H:C = 1.66), the organic density was obtained from the parameterization of *Kuwata et al.*, $\rho_{org}$ = (12 + H:C + 16 O:C) / (7.0 + 5.0 H:C + 4.15 O:C) = 1.21 g cm$^{-3}$ (Kuwata et al., 2012). Combining the organic fraction with the inorganic fraction yields a bulk density of $\rho_p = 1.37$ g cm$^{-3}$.

Applying Eq. S1, the AMS peak-transmission window of ≈50–500 nm in $d_{va}$ corresponds to roughly 37–366 nm in $d_m$, which lies entirely within the FIMS measurement range of 10–600 nm (Wang et al., 2018; Liu et al., 2007). Moreover, the dry critical diameters governing activation at the two operating supersaturations are $D_{crit} \approx$ 54–133 nm across $\kappa = 0.1$–$0.4$ fall inside this 37–366 nm overlap. The bulk AMS composition is therefore representative of the FIMS-measured particles at the diameters that control CCN activation, justifying the use of the FIMS distribution together with the AMS composition in the closure analysis.

## Section S2. HR-ToF-AMS Analysis Methodology

In order to analyze the raw HR-ToF-AMS files, the ToF AMS Analysis Kit 1.66 program is used in Igor Pro (WaveMetrics Inc., version 9.05). The AMS data analysis was performed following the standard protocols described elsewhere (Canagaratna et al., 2015; Middlebrook et al., 2012). The steps in running HR-ToF-AMS data analysis begins with the blacklisting of negative air beam values, removing bad points. Mass calibration on the full data set is then run with masses that have consistent peak fits. After a few more steps to optimize the dataset, the peak shape in confirmed for all peaks. Then, all the masses are fit from m/z 12 to 200, hand selected one peak at a time. Based on peak fittings of all the masses, and HR fit of all the peaks based on the peak shape is done. After this HR fitting has been completed, O:C and H:C ratios can be drawn out through Elemental Analysis (Canagaratna et al., 2015). These are the O:C and H:C ratios applied in Section 3.4 analysis. With all the HR fittings done, the results can be exported to an .itx file for PMF analysis, which is discussed in both Section 2.3.3 and Section S3.

## Section S3. Positive Matrix Factorization (PMF/ME-2): Inputs, Preprocessing, and Solution Diagnostics

### S 3.1 Input data and uncertainty matrices

Source apportionment was performed on a combined organic–inorganic–size data matrix of 372 five-minute-averaged samples. The variable set comprised 96 organic ion signals (*m/z* 12–120), the four non-refractory inorganic species measured by the HR-ToF-AMS, and the FIMS mobility size distribution together with the integrated number concentration and geometric mean diameter, all shown in Table S3. A corresponding uncertainty matrix of identical dimensions was assembled from the AMS ion-level error estimates and the FIMS bin-to-bin variability (the 5-min standard deviation).

### S 3.2 Preprocessing

Raw HR-ToF-AMS and FIMS data were resampled to a common 5-min time base and aligned to the timestamps for which both instruments reported valid data, and intervals lacking FIMS coverage were removed. Columns that included zero values over the campaign were dropped.

### S 3.3 Treatment of weak and bad variables

Organic ions with a signal-to-noise ratio (SNR) below 0.2 were classified as "bad" and excluded, and ions with $0.2 \leq \mathrm{SNR} \leq 2$ were classified as "weak" and downweighted by a factor of 2, increasing their error estimates (Paatero and Hopke, 2003; Ulbrich et al., 2009). The combined matrix mixes organic spectra with inorganic mass concentrations and the size distribution, so the inorganic and size variables were additionally downweighted relative to the organic signal so that their larger magnitudes did not outweigh the organic mass spectrum. The

downweighting factor for the inorganic masses was scaled by the campaign *m/z* 44 signal (normalized to their 95th percentiles) (Nursanto et al., 2023).

### S 3.4 Number of factors and $Q/Q_{exp}$

Solutions were explored with both the Igor PMF Evaluation Tool (PET) and the ME-2 engine, with ME-2 runs computed from one through ten factors, shown in Table S4. The number of factors was chosen based on the $Q/Q_{exp}$ ratio together with the physical interpretability and cross-engine reproducibility of the resolved factors. $Q/Q_{exp}$ decreased monotonically with added factors, from 17.5 (one factor) to 7.7 (three), 6.7 (four), and 4.6 (five), reaching 2.9 at ten factors, while the explained variation rose steeply to 78% by three factors and then plateaued, shown in Figure S11. Based on a levelling off of explained variation and the consistency of factors in the ME-2 four-factor run, the four-factor ME-2 solution was considered the robust solution. From here forward, the only solution mentioned will be the four-factor ME-2 solution.

### S 3.5 ME-2 constraints and a-values

In the ME-2 runs, factor profiles were guided toward reference organic-aerosol mass spectra using the a-value approach, which limits the deviation of the constrained profiles from the reference while allowing the factor time series to vary freely, and no *fpeak* rotations were applied. The final four-factor solutions used an a-value of 0.25 for the Spring campaign and 0.5 for the Fall campaign, with the profiles anchored to reference spectra (Mohr et al., 2012).

### S 3.6 Residuals and unexplained mass

Model performance was evaluated from the residuals, $e_{ij} = S_{ij} - (G \cdot F)_{ij}$, the difference between the measured and reconstructed signal of ion *j* at time *i*. For the final four-factor solution the reconstruction reproduced the measured signal well with a correlation coefficient

0.91, and the four factors together explained 84.7% of the total measured variance, leaving roughly 15% of the signal unexplained. The distribution of the scaled residuals and the residual time series are shown in Figure S12. The scaled residuals are approximately centered on zero, and no individual m/z or time period dominates the residual, indicating that the four-factor solution captures the variability in the dataset without a structured, unmodeled component.

**S 3.7 Factor time series, contributions, and correlations**

The four ME-2 factors and their temporal behavior are shown in Figure 5 of the main text. Pearson correlations among the four factor time series in Figure S13 were low except between the two oxygenated factors, indicating that the factors capture largely independent temporal behavior.

## Section S4. Statistical Methods of Seasonal Organic Hygroscopicity

To test whether the modeled organic hygroscopicity differed between the Spring and Fall periods within each air-mass region, $\kappa_{org}$ was first averaged to a single value per research flight for each region, so that the sampling unit is an independent flight rather than an individual one-minute record. This is necessary because the values of $\kappa_{org}$ values within a flight are strongly autocorrelated. If they were to be treated as independent variables, it would inflate the effective sample size by two to three orders of magnitude and result in artificially small $p$-values. A two-sample Welch's $t$-test was then applied to the per-flight Spring and Fall $\kappa_{org}$ values for each region (Welch, 1947). The comparison was carried out independently for each of the four $\kappa_{org}$ estimates, being both mixing states and supersaturations, and a difference was considered statistically significant at $p < 0.05$. Regions with fewer than two flights in a season were not tested. The Southeast had no Spring flights and thus is ineligible for interseason comparisons.

Across all regions and $\kappa_{org}$ estimates, no seasonal difference reached the $p < 0.05$ threshold (all $p > 0.17$), and every 95% confidence interval on the seasonal difference included zero. These results are shown in Table S5. The regional seasonal differences apparent in Figure 2 are therefore not statistically distinguishable at the flight level given the available number of flights, and seasonal differences are discussed as qualitative instead of quantitative.

It should be noted that the Fall period includes only two to three flights per region, so the statistical power of this comparison is limited. A non-significant result therefore indicates that a seasonal difference could not be resolved with the number of available flights, not that $\kappa_{org}$ is necessarily equal between seasons.

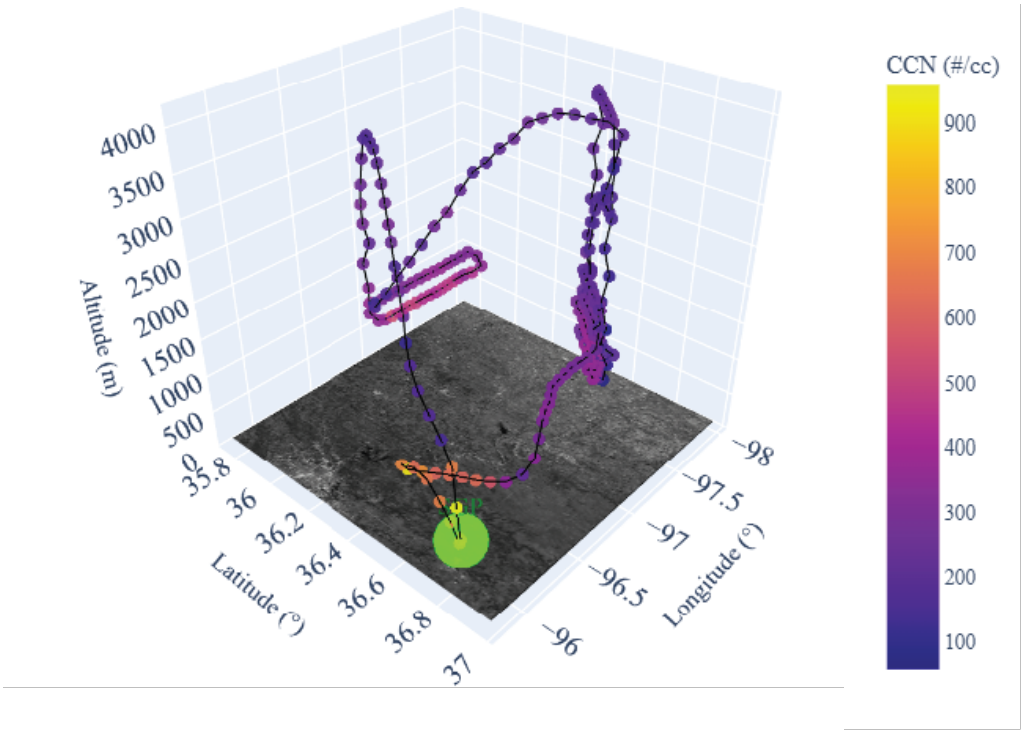



**Figure S1.** A representation of one flight during the campaign, displaying CCN counts at different heights.

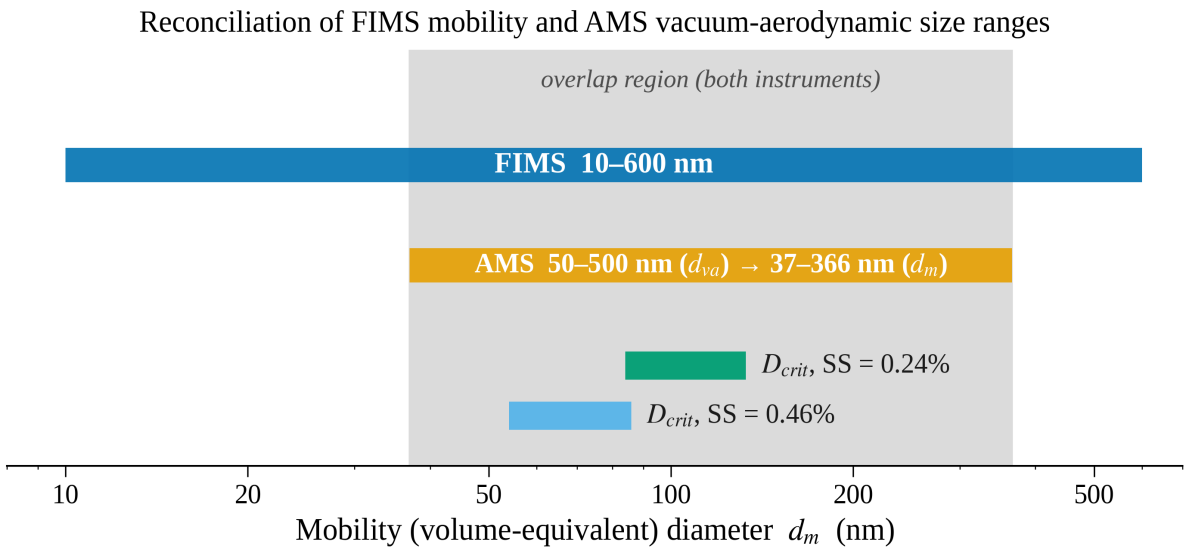
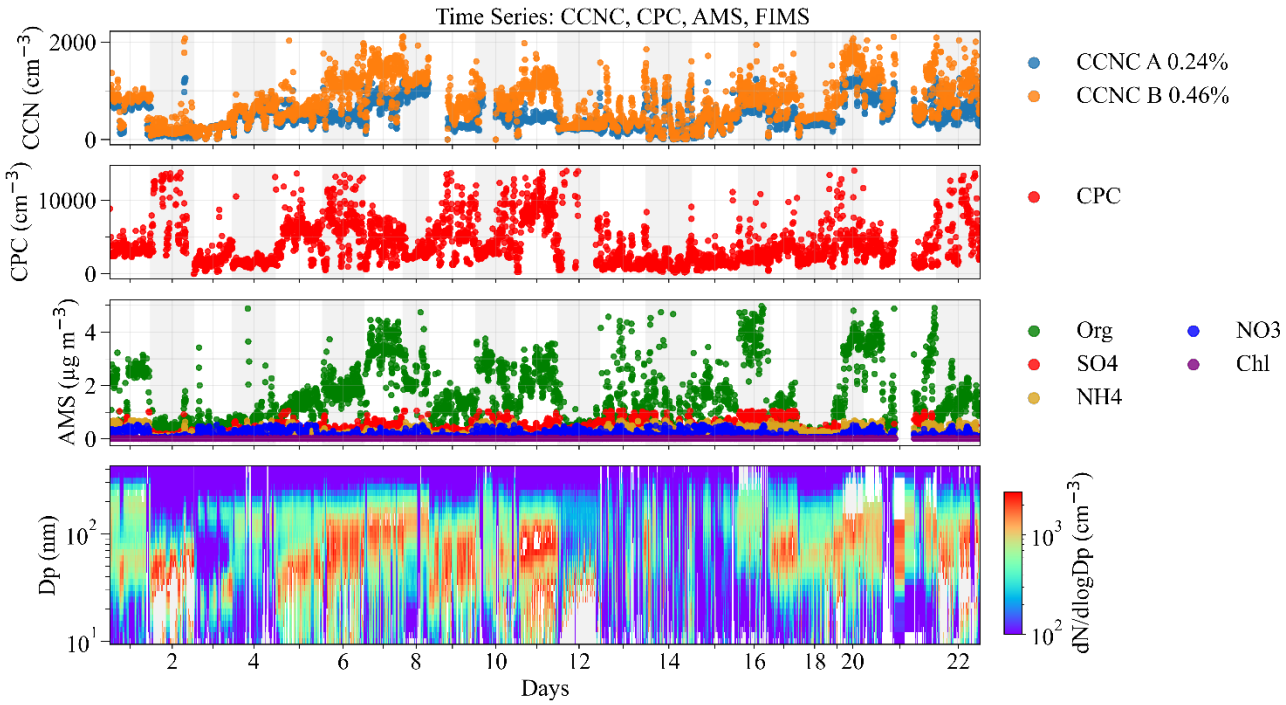



**Figure S2.** Reconciliation of the FIMS and HR-ToF-AMS size ranges on a common mobility-diameter axis. The AMS peak-transmission window is shown in gold, while the FIMS range is shown in blue. The dry critical diameters at SS = 0.24% and 0.46% (for $\kappa$ = 0.1–0.4) fall inside the overlap region (gray), confirming that both instruments robustly characterize the particles at the sizes that control CCN activation.




149

150 **Figure S3.** The full time series of the flight campaign. The top panel is CCN concentrations,

151 the second panel is CPC concentrations, the third panel is AMS mass loadings, and the fourth

152 panel is FIMS size distributions.

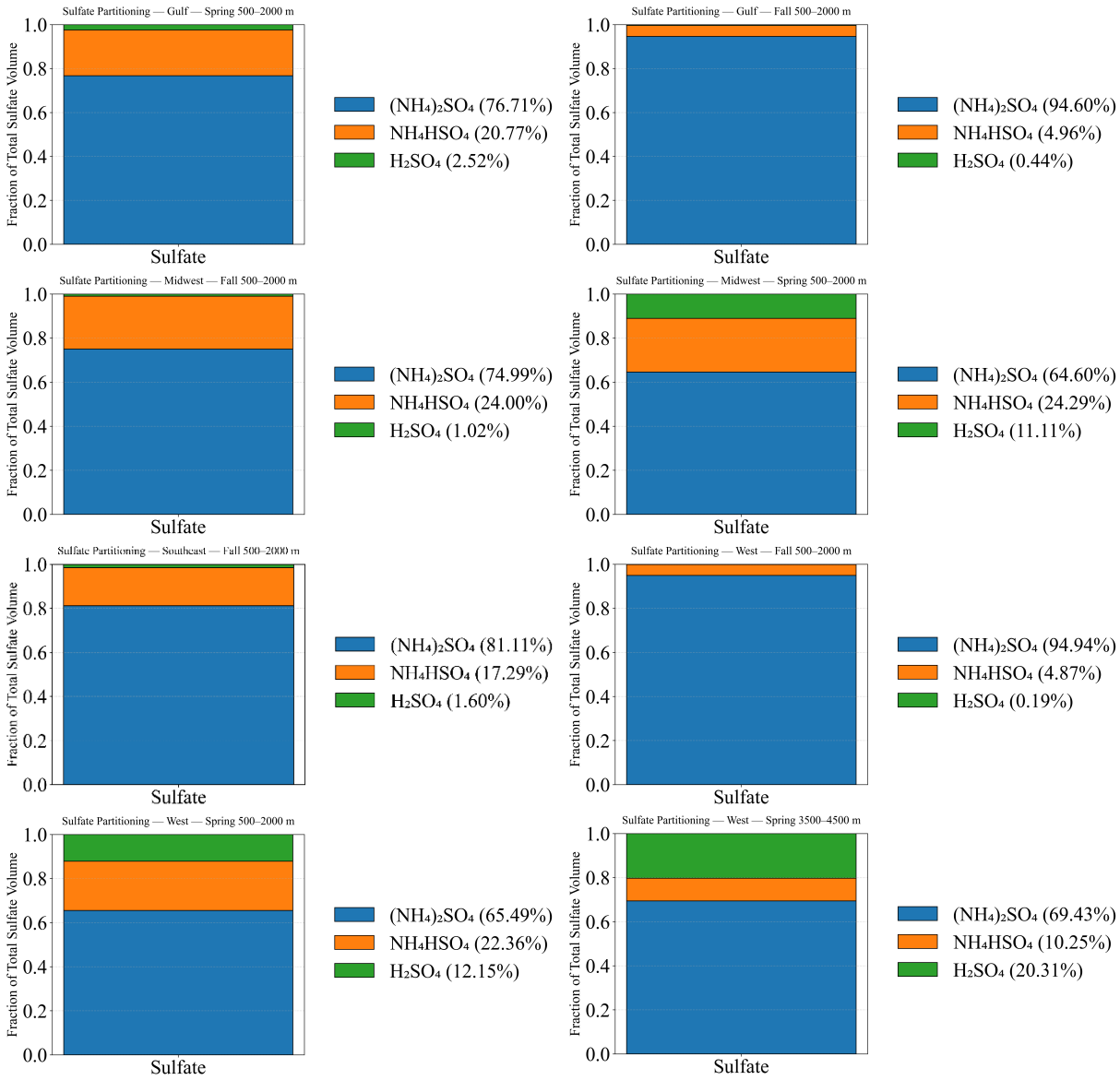
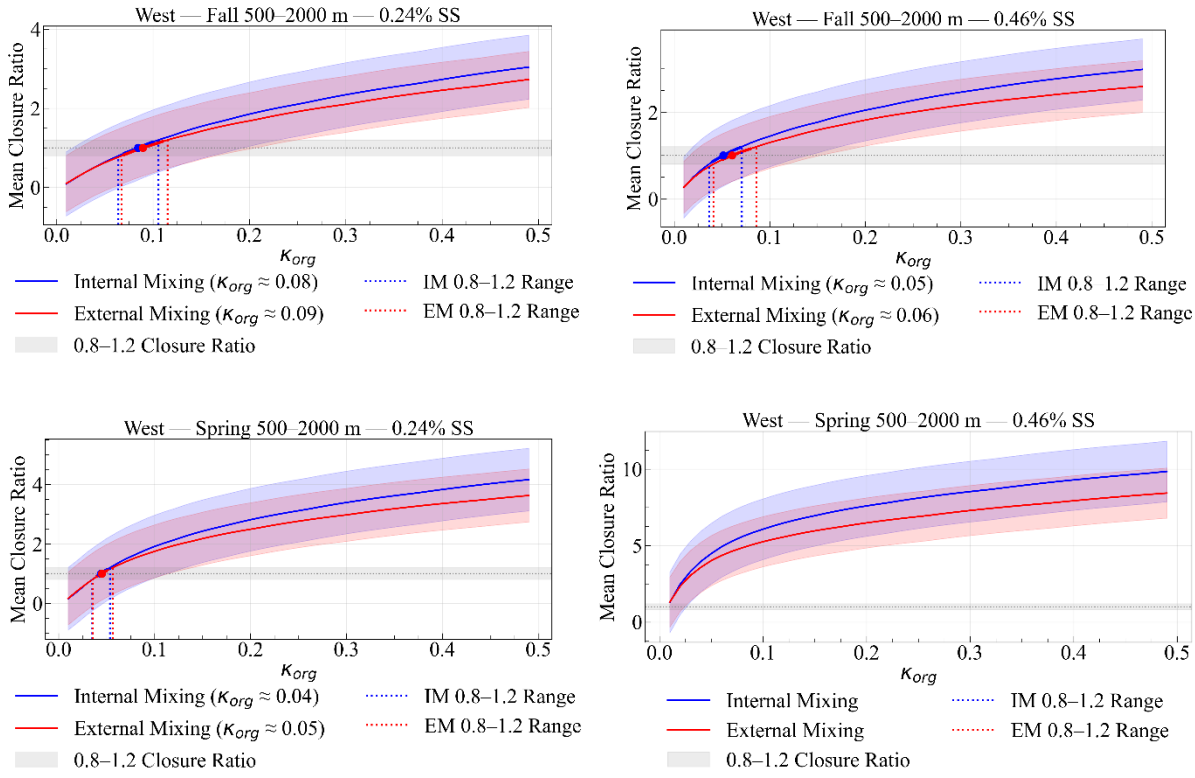



**Figure S4.** The partitioning of sulfate species for each region, season and height, with ammonium sulfate in blue, ammonium bisulfate in orange, and sulfuric acid in green.

158

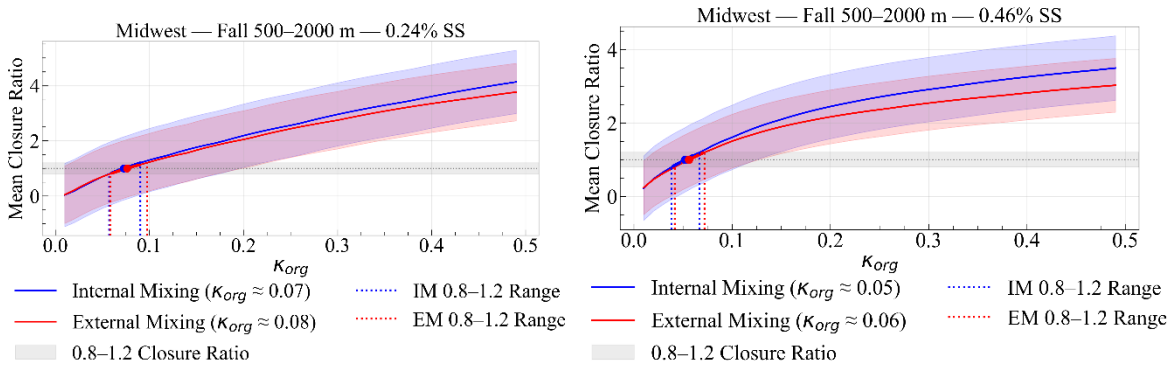



159

160 **Figure S5.** Closure curves of the West region, broken down by season and supersaturation.
161 Shaded around each curve is ±1 standard deviation and shaded in gray is the closure ratio value
162 between 0.8 and 1.2. Within each legend is the modeled organic hygroscopicity rounded to the
163 hundredths.

164

165




166

167 **Figure S6.** Closure curves of the Midwest region, broken down by season and supersaturation.

168 Shaded around each curve is ±1 standard deviation and shaded in gray is the closure ratio value

169 between 0.8 and 1.2. Within each legend is the modeled organic hygroscopicity rounded to the

170 hundredths.

171

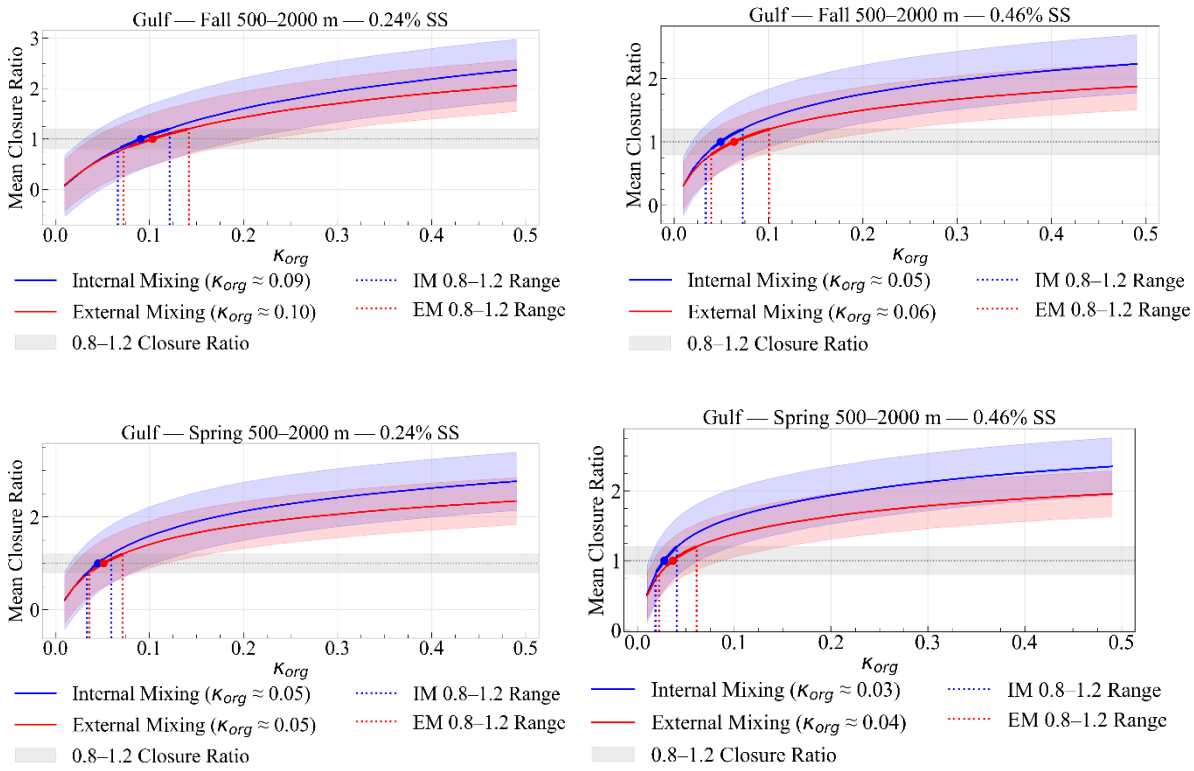



**Figure S7.** Closure curves of the Gulf region, broken down by season and supersaturation. Shaded around each curve is ±1 standard deviation and shaded in gray is the closure ratio value between 0.8 and 1.2. Within each legend is the modeled organic hygroscopicity rounded to the hundredths.

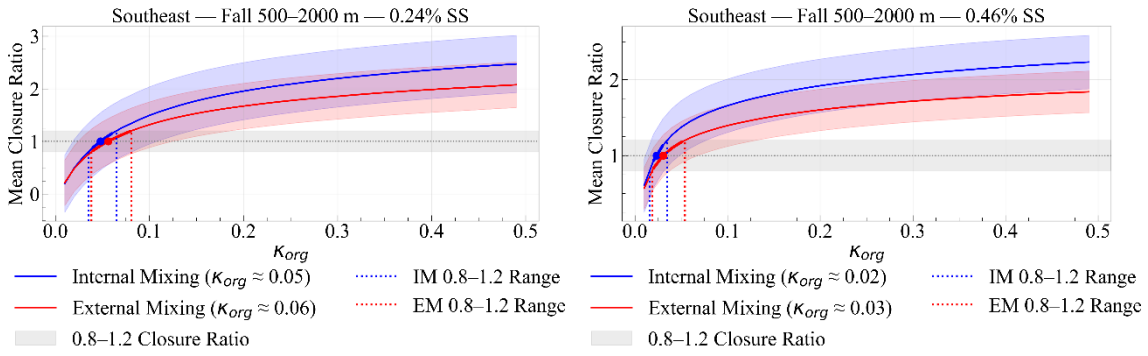



**Figure S8.** Closure curves of the Southeast region, broken down by season and supersaturation. Shaded around each curve is ±1 standard deviation and shaded in gray is the closure ratio value between 0.8 and 1.2. Within each legend is the modeled organic hygroscopicity rounded to the hundredths.

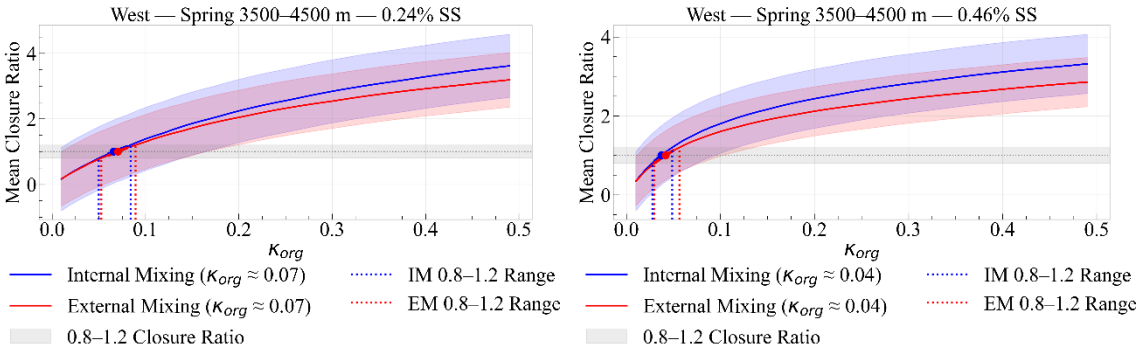
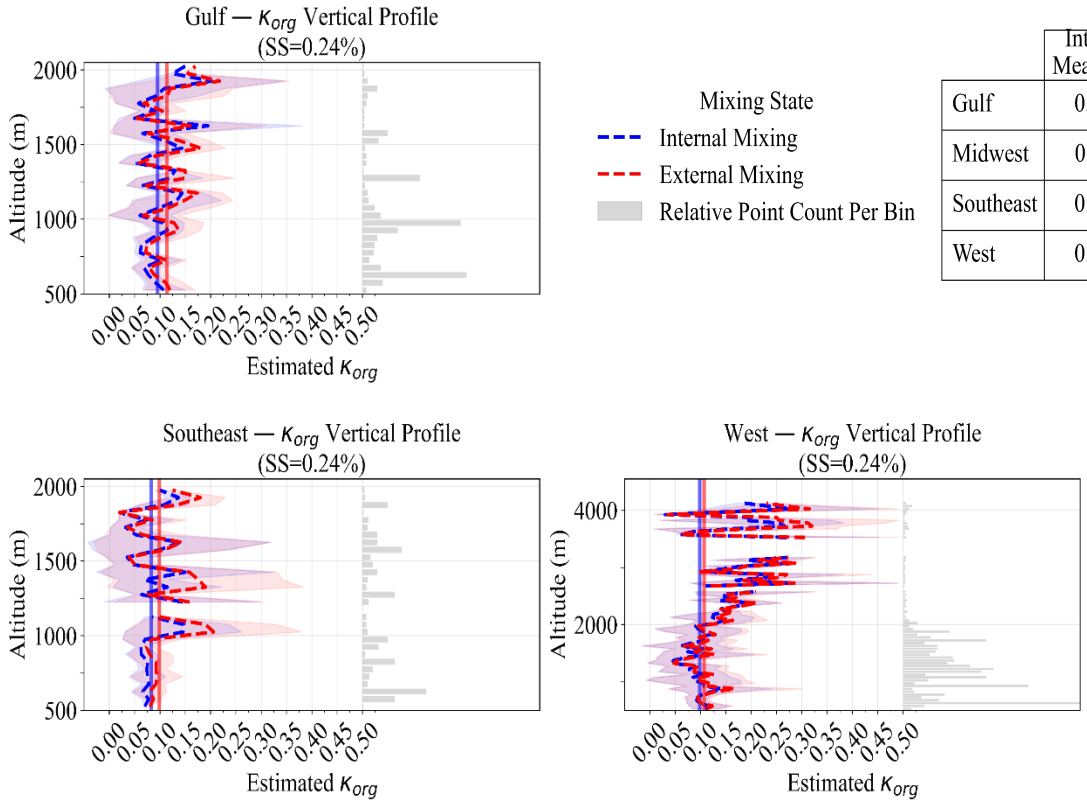



**Figure S9.** Closure curves of the West region, broken down by supersaturation, and specifically in the altitude between 3500 and 4500 m. Shaded around each curve is ±1 standard deviation and shaded in gray is the closure ratio value between 0.8 and 1.2. Within each legend is the modeled organic hygroscopicity rounded to the hundredths.



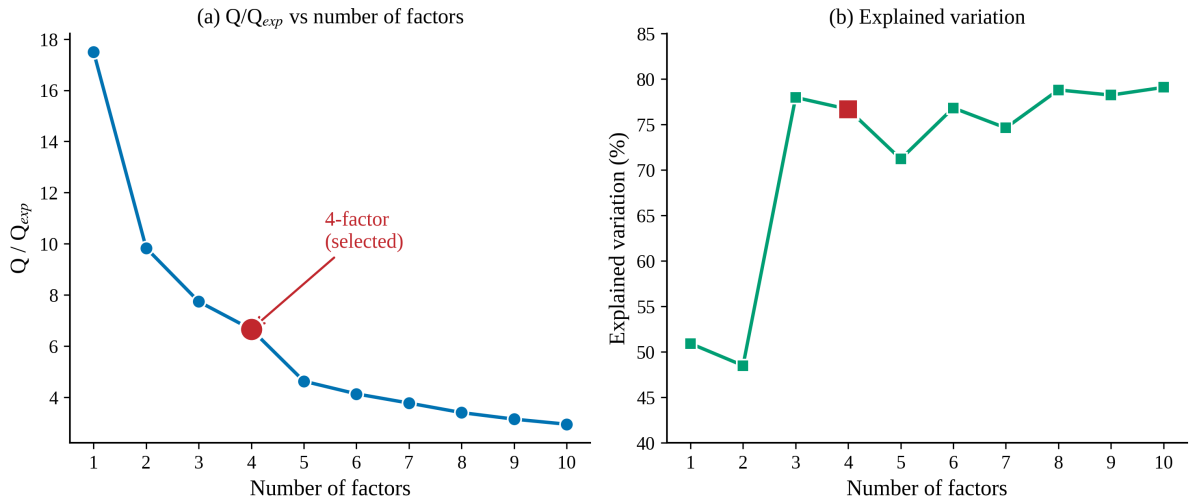

| | Internal Mean $\kappa_{org}$ | External Mean $\kappa_{org}$ |
|---|---|---|
| Gulf | 0.095 | 0.113 |
| Midwest | 0.113 | 0.125 |
| Southeast | 0.083 | 0.099 |
| West | 0.098 | 0.107 |

192

193 **Figure S10.** The other three vertical profiles from the methodology in Section 2.3.2, all at the

194 atmospherically relevant supersaturation of 0.24%.

195




196

197 **Figure S11.** (a) $Q/Q_{exp}$ and (b) explained variation as a function of the number of ME-2 factors

198 (solved runs, 1–10 factors); the four-factor solution (red) is the selected solution.

199

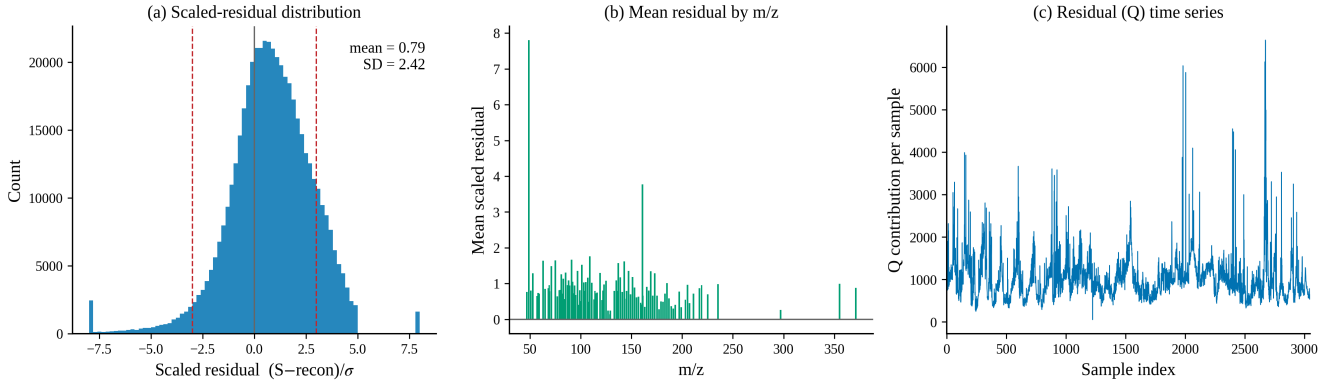
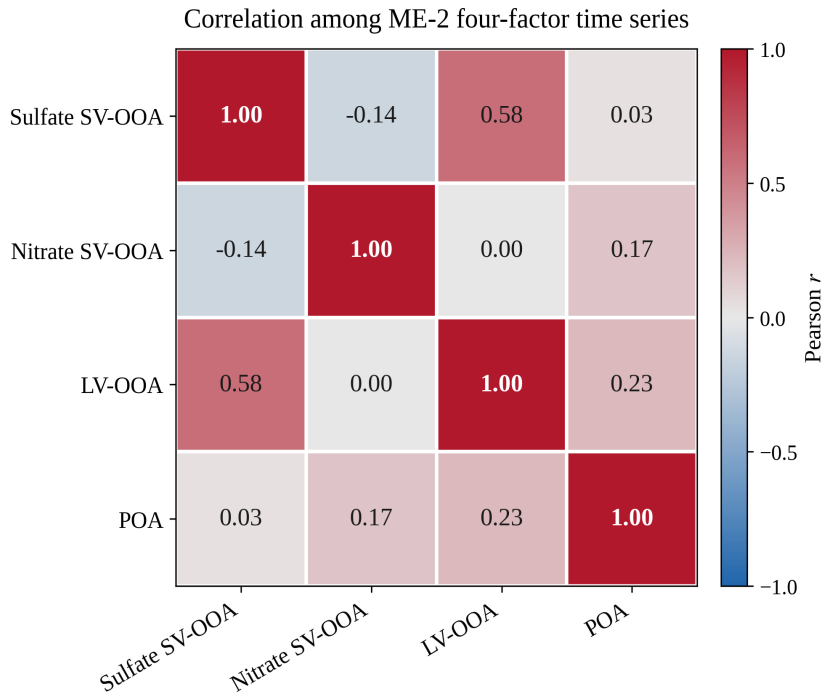



**Figure S12.** Residual diagnostics for the four-factor ME-2 solution. (a) distribution of scaled residuals, (b) mean scaled residual by m/z, and (c) residual (Q-contribution) per sample.




204

205 **Figure S13.** Pearson correlation coefficients among the four ME-2 factor time series (n = 368).

206

**Table S1.** Summary of the HI-SCALE research flights used in this study. The 22 flight days (15 in Spring, 7 in Fall) are those retained after data cleaning with concurrent CCN, CPC, FIMS, and HR-ToF-AMS measurements. "Sampling (min)" denotes the number of 1-min records for which all four instruments reported valid data.

| Season | Flight | Date | Sampling (min) | Altitude bands (km) |
|---|---|---|---|---|
| Spring | 1 | 25 Apr 2016 | 198 | 0.5–1, 1–2 |
| | 2 | 28 Apr 2016 | 210 | 0.5–1, 1–2 |
| | 3 | 1 May 2016 | 188 | 0.5–1, 1–2 |
| | 4 | 2 May 2016 | 208 | 0.5–1, 1–2 |
| | 5 | 3 May 2016 | 231 | 0.5–1, 1–2 |
| | 6 | 6 May 2016 | 199 | 0.5–1, 1–2 |
| | 7 | 7 May 2016 | 192 | 0.5–1, 1–2 |
| | 8 | 8 May 2016 | 125 | 0.5–1, 1–2 |
| | 9 | 10 May 2016 | 230 | 0.5–1, 1–2 |
| | 10 | 11 May 2016 | 190 | 0.5–1, 1–2 |
| | 11 | 13 May 2016 | 210 | 0.5–1, 1–2 |
| | 12 | 14 May 2016 | 202 | 0.5–1, 1–2 |
| | 13 | 16 May 2016 | 226 | 0.5–1, 1–2, 3.5–4.5 |
| | 14 | 19 May 2016 | 220 | 0.5–1, 1–2, 3.5–4.5 |
| | 15 | 20 May 2016 | 229 | 0.5–1, 1–2 |
| Fall | 16 | 29 Aug 2016 | 153 | 0.5–1, 1–2 |
| | 17 | 9 Sep 2016 | 133 | 0.5–1, 1–2 |
| | 18 | 10 Sep 2016 | 169 | 0.5–1, 1–2 |
| | 19 | 11 Sep 2016 | 51 | 0.5–1, 1–2 |
| | 20 | 13 Sep 2016 | 102 | 0.5–1, 1–2 |
| | 21 | 15 Sep 2016 | 267 | 0.5–1, 1–2 |
| | 22 | 17 Sep 2016 | 212 | 0.5–1, 1–2 |

212 **Table S2.** Hygroscopicity values used for Eq. 4 calculations (Petters and Kreidenweis, 2007;
213 Seinfeld and Pandis, 2016).

| Compound | $(NH_4)_2SO_4$ | $NH_4HSO_4$ | $H_2SO_4$ | $NH_4NO_3$ | $NH_4Cl$ |
|---|---|---|---|---|---|
| Hygroscopicity | 0.61 | 0.45 | 0.90 | 0.67 | 0.65 |

214

**Table S3.** Composition of the PMF input matrix (372 five-minute samples).

| Variable group | No. | Notes |
|---|---|---|
| Organic ions (HR-ToF-AMS) | 96 | m/z 12–120, high-resolution |
| Inorganic species totals | 4 | sulfate, nitrate, ammonium, chloride |
| FIMS size-distribution bins | 30 | 9.4–426 nm (mobility) |
| Integrated / derived | 2 | total number, geometric mean diameter |

**Table S4.** PMF/ME-2 solutions evaluated.

| Engine | No. factors | Factors resolved |
|---|---|---|
| PET | 3 | SV-OOA, LV-OOA, HOA/BBOA |
| ME-2 | 3 | SV-OOA, POA, size-distribution |
| ME-2 | **4 (final)** | Sulfate SV-OOA, Nitrate SV-OOA, LV-OOA, POA |
| PET | 5 | Sulfate SV, Nitrate SV, SV-OOA, LV-OOA, size-dist. |
| ME-2 | 5 | Sulfate LV, Nitrate LV, SV-OOA, OOA, POA |

**Table S5.** Flight-level Welch's t-test of Spring vs. Fall $\kappa_{org}$ by region. Values are mean ± 1 standard error across flights; Δ is the season difference with its 95% confidence interval.

| Region | Estimate | n (Spr/Fall) | κ_org Spring | κ_org Fall | Δ (Fall − Spr) [95% CI] | p |
|---|---|---|---|---|---|---|
| West | Internal 0.24% | 10 / 3 | 0.112 ± 0.019 | 0.105 ± 0.005 | -0.007 [-0.051, +0.036] | 0.73 |
| | External 0.24% | 10 / 3 | 0.127 ± 0.022 | 0.113 ± 0.004 | -0.013 [-0.064, +0.038] | 0.57 |
| | Internal 0.46% | 10 / 3 | 0.059 ± 0.011 | 0.070 ± 0.008 | +0.011 [-0.019, +0.041] | 0.44 |
| | External 0.46% | 10 / 3 | 0.074 ± 0.014 | 0.079 ± 0.008 | +0.006 [-0.030, +0.041] | 0.74 |
| Midwest | Internal 0.24% | 8 / 2 | 0.112 ± 0.015 | 0.128 ± 0.034 | +0.016 [-0.231, +0.263] | 0.72 |
| | External 0.24% | 8 / 2 | 0.124 ± 0.019 | 0.134 ± 0.034 | +0.010 [-0.189, +0.208] | 0.83 |
| | Internal 0.46% | 8 / 2 | 0.056 ± 0.010 | 0.075 ± 0.007 | +0.019 [-0.011, +0.050] | 0.17 |
| | External 0.46% | 8 / 2 | 0.068 ± 0.013 | 0.087 ± 0.011 | +0.019 [-0.026, +0.064] | 0.33 |
| Gulf | Internal 0.24% | 5 / 2 | 0.094 ± 0.014 | 0.104 ± 0.015 | +0.010 [-0.056, +0.076] | 0.66 |
| | External 0.24% | 5 / 2 | 0.112 ± 0.018 | 0.118 ± 0.013 | +0.007 [-0.052, +0.065] | 0.77 |
| | Internal 0.46% | 5 / 2 | 0.052 ± 0.008 | 0.060 ± 0.017 | +0.008 [-0.111, +0.127] | 0.72 |
| | External 0.46% | 5 / 2 | 0.067 ± 0.009 | 0.077 ± 0.016 | +0.009 [-0.085, +0.104] | 0.66 |
| Southeast | Internal 0.24% | 0 / 2 | — (no Spring) | 0.083 ± 0.001 | not testable | — |
| | External 0.24% | 0 / 2 | — (no Spring) | 0.098 ± 0.003 | not testable | — |
| | Internal 0.46% | 0 / 2 | — (no Spring) | 0.048 ± 0.002 | not testable | — |
| | External 0.46% | 0 / 2 | — (no Spring) | 0.065 ± 0.002 | not testable | — |

## References


Canagaratna, M. R., Jimenez, J. L., Kroll, J. H., Chen, Q., Kessler, S. H., Massoli, P., Hildebrandt Ruiz, L., Fortner, E., Williams, L. R., Wilson, K. R., Surratt, J. D., Donahue, N. M., Jayne, J. T., and Worsnop, D. R.: Elemental ratio measurements of organic compounds using aerosol mass spectrometry: characterization, improved calibration, and implications, Atmos. Chem. Phys., 15, 253–272, 10.5194/acp-15-253-2015, 2015.

DeCarlo, P. F., Slowik, J. G., Worsnop, D. R., Davidovits, P., and Jimenez, J. L.: Particle Morphology and Density Characterization by Combined Mobility and Aerodynamic Diameter Measurements. Part 1: Theory, Aerosol Science and Technology, 38, 1185–1205, 10.1080/027868290903907, 2004.

Kuwata, M., Zorn, S. R., and Martin, S. T.: Using Elemental Ratios to Predict the Density of Organic Material Composed of Carbon, Hydrogen, and Oxygen, Environmental Science & Technology, 46, 787–794, 10.1021/es202525q, 2012.

Liu, P. S. K., Deng, R., Smith, K. A., Williams, L. R., Jayne, J. T., Canagaratna, M. R., Moore, K., Onasch, T. B., Worsnop, D. R., and Deshler, T.: Transmission Efficiency of an Aerodynamic Focusing Lens System: Comparison of Model Calculations and Laboratory Measurements for the Aerodyne Aerosol Mass Spectrometer, Aerosol Science and Technology, 41, 721–733, 10.1080/02786820701422278, 2007.

Middlebrook, A. M., Bahreini, R., Jimenez, J. L., and Canagaratna, M. R.: Evaluation of Composition-Dependent Collection Efficiencies for the Aerodyne Aerosol Mass Spectrometer using Field Data, Aerosol Science and Technology, 46, 258–271, 10.1080/02786826.2011.620041, 2012.

Mohr, C., DeCarlo, P. F., Heringa, M. F., Chirico, R., Slowik, J. G., Richter, R., Reche, C., Alastuey, A., Querol, X., Seco, R., Peñuelas, J., Jiménez, J. L., Crippa, M., Zimmermann, R., Baltensperger, U., and Prévôt, A. S. H.: Identification and quantification of organic aerosol from cooking and other sources in Barcelona using aerosol mass spectrometer data, Atmos. Chem. Phys., 12, 1649–1665, 10.5194/acp-12-1649-2012, 2012.

Nursanto, F. R., Meinen, R., Holzinger, R., Krol, M. C., Liu, X., Dusek, U., Henzing, B., and Fry, J. L.: What chemical species are responsible for new particle formation and growth in the Netherlands? A hybrid positive matrix factorization (PMF) analysis using aerosol composition (ACSM) and size (SMPS), Atmos. Chem. Phys., 23, 10015–10034, 10.5194/acp-23-10015-2023, 2023.

Paatero, P. and Hopke, P. K.: Discarding or downweighting high-noise variables in factor analytic models, Analytica Chimica Acta, 490, 277–289, https://doi.org/10.1016/S0003-2670(02)01643-4, 2003.

Petters, M. D. and Kreidenweis, S. M.: A single parameter representation of hygroscopic growth and cloud condensation nucleus activity, Atmos. Chem. Phys., 7, 1961–1971, 10.5194/acp-7-1961-2007, 2007.

Seinfeld, J. H. and Pandis, S. N.: Atmospheric chemistry and physics: from air pollution to climate change, John Wiley & Sons2016.

Ulbrich, I. M., Canagaratna, M. R., Zhang, Q., Worsnop, D. R., and Jimenez, J. L.: Interpretation of organic components from Positive Matrix Factorization of aerosol mass spectrometric data, Atmos. Chem. Phys., 9, 2891–2918, 10.5194/acp-9-2891-2009, 2009.

Wang, Y., Pinterich, T., and Wang, J.: Rapid measurement of sub-micrometer aerosol size distribution using a fast integrated mobility spectrometer, Journal of Aerosol Science, 121, 12–20, https://doi.org/10.1016/j.jaerosci.2018.03.006, 2018.

Welch, B. L.: The generalization of 'Student's' problem when several different population variances are involved, Biometrika, 34, 28–35, 10.1093/biomet/34.1-2.28, 1947.